

RESEARCH ARTICLE

Locomotor benefits of being a slender and slick sand swimmer

Sarah S. Sharpe^{1,2}, Stephan A. Koehler³, Robyn M. Kuckuk², Miguel Serrano⁴, Patricio A. Vela⁴, Joseph Mendelson, III⁵ and Daniel I. Goldman^{1,6,*}

ABSTRACT

Squamates classified as ‘subarenaceous’ possess the ability to move long distances within dry sand; body elongation among sand and soil burrowers has been hypothesized to enhance subsurface performance. Using X-ray imaging, we performed the first kinematic investigation of the subsurface locomotion of the long, slender shovel-nosed snake (*Chionactis occipitalis*) and compared its biomechanics with those of the shorter, limbed sandfish lizard (*Scincus scincus*). The sandfish was previously shown to maximize swimming speed and minimize the mechanical cost of transport during burial. Our measurements revealed that the snake also swims through sand by propagating traveling waves down the body, head to tail. Unlike the sandfish, the snake nearly followed its own tracks, thus swimming in an approximate tube of self-fluidized granular media. We measured deviations from tube movement by introducing a parameter, the local slip angle, β_s , which measures the angle between the direction of movement of each segment and body orientation. The average β_s was smaller for the snake than for the sandfish; granular resistive force theory (RFT) revealed that the curvature utilized by each animal optimized its performance. The snake benefits from its slender body shape (and increased vertebral number), which allows propagation of a higher number of optimal curvature body undulations. The snake’s low skin friction also increases performance. The agreement between experiment and RFT combined with the relatively simple properties of the granular ‘frictional fluid’ make subarenaceous swimming an attractive system to study functional morphology and bauplan evolution.

KEY WORDS: Undulatory locomotion, Granular media, Resistive force theory, Snake, Lizard, Subsurface

INTRODUCTION

The prediction of locomotor performance in relation to features of body morphology (body shape, skin properties and limb number) is a topic of interest from bio/neuromechanical (Aristotle, 350 BCE; Dayton et al., 2005; Gans, 1975; Mosauer, 1932; Russell, 1917; Tytell et al., 2010; Wainwright and Reilly, 1994) and robotic perspectives (Brooks, 1992; Lauder et al., 2007; Maladen et al., 2011a; Maladen et al., 2011c; Pfeifer et al., 2007; Yim et al., 2007). From an evolutionary perspective, it is important to quantitatively address questions associated with putative selective pressures for locomotor apparatus and bauplans in different environments

(Lauder, 1981; Lauder and Drucker, 2004; Walker and Westneat, 2000). Such studies are necessarily complicated because body morphology, kinematics and environment interactions are typically strongly coupled.

Much progress in disentangling these factors has been made in the studies of locomotion in fluids. For example, in swimming, using a variety of tools [(e.g. high-speed imaging, particle image velocimetry (Drucker and Lauder, 1999)], many biological studies have been conducted to understand how aspects of morphology [e.g. effects of body shape, limb shape and stiffness (Fish and Battle, 1995; Long and Nipper, 1996; Miklosovic et al., 2004)] and movement mechanics (Blake, 2004; Fish and Lauder, 2006; Liao, 2007; Sfakiotakis et al., 1999) contribute to performance. Such systems have also been the focus of models that allow systematic understanding by linking shape to function, through probing of fluid–structure interactions and how aspects of morphology affect performance. These modeling approaches include mathematical and computational (Alexander, 2003; Anderson and Wendt, 1995; Lighthill, 1971; Liu et al., 1996; McHenry and Jed, 2003; Pedley and Hill, 1999; Tytell and Lauder, 2004; Webb and Weihs, 1986) modeling using the Navier–Stokes equations of fluid dynamics, as well as a more recent modeling approach, using physical robot swimming and flying models (Brooks, 1992; Lauder et al., 2007; Maladen et al., 2011a; McHenry et al., 1995; Yim et al., 2007).

Seemingly complex dry granular environments (which display solid and fluid-like aspects) are also amenable to detailed experiment/theory comparison (Ding et al., 2012; Ding et al., 2013; Maladen et al., 2011b). High-speed X-ray imaging and EMG studies of the biomechanical and neuromechanical aspects of the sand swimming sandfish lizard, *Scincus scincus* (Linnaeus), a ‘subarenaceous’ animal (Mosauer, 1932) (living within sand and swimming for long distances) native to the Sahara Desert (Fig. 1C) have provided insight into the locomotor strategy and performance of this sand swimmer, and have even revealed principles of swimmers in real fluids (Ding et al., 2013). X-ray imaging of the sandfish lizard (Maladen et al., 2009; Sharpe et al., 2013) revealed that it swims subsurface using single-period anterior-to-posterior traveling body curvature waves while its limbs remain along its body. A multi-particle discrete element method (DEM) simulation of a granular material (composed of 3 mm diameter particles) coupled to a numerical model of the animal captured swimming kinematics and predicted that sandfish swimming takes place within a self-generated localized ‘frictional fluid’ (Ding et al., 2012). However, because of the high computational time, DEM could not be used to study locomotion in smaller particle natural substrates.

A granular resistive force theory (RFT) was developed (Ding et al., 2012; Maladen et al., 2009; Maladen et al., 2011b) to gain insight into the principles of sand swimming in more natural environments. In RFT, a body is partitioned into infinitesimal segments, each experiencing thrust and drag related to the orientation and environmental interaction. RFT assumes forces on a particular segment are independent of forces from neighboring

¹Interdisciplinary Bioengineering Program, Georgia Tech, Atlanta, GA 30332-0363, USA. ²Department of Biomedical Engineering, Georgia Tech, Atlanta, GA 30332-0363, USA. ³School of Engineering and Applied Sciences, Harvard University, Cambridge, MA 02138, USA. ⁴Department of Electrical and Computer Engineering, Georgia Tech, Atlanta, GA 30332-0363, USA. ⁵Zoo Atlanta and School of Biology, Georgia Tech, Atlanta, GA 30332-0363, USA. ⁶School of Physics, Georgia Tech, Atlanta, GA 30332-0363, USA.

*Author for correspondence (daniel.goldman@physics.gatech.edu)

Received 20 May 2014; Accepted 6 November 2014

List of symbols and abbreviations

CoT	cost of transport
CP	closely packed
DEM	discrete element method
L	effective body length
LP	loosely packed
L/λ_s	local undulation number
m	body marker location
\hat{N}	normal unit vector
r	radius
RFT	resistive force theory
s	arc length
STL	snout–tail length
SVL	snout–vent length
t	time
\hat{T}	tangent vector
\hat{v}	unit velocity vector
v_c	velocity of the curvature wave
w	average body width
W	winding number
β_s	slip angle
$\bar{\beta}_s$	spatial and temporal average of the slip angle
η_u	undulatory efficiency
θ_{slide}	inclination angle at which the animal begins to slide
κ_{max}	maximum bending curvature
κ/λ_s	relative curvature
$\overline{\kappa/\lambda_s}$	mean relative curvature
$\lambda_{s/2}$	half-arc length
μ_s	body–particle friction
ξ	undulation number
$\bar{\xi}$	mean undulation number
ρ	particle material density
ϕ	volume fraction

segments. Net forward thrust is determined by integrating forces over all body segments. With empirically measured force relationships (Maladen et al., 2009) (the granular equivalent of Stokes' laws), the granular RFT allowed us to make accurate statements about sandfish swimming kinematics and performance. The model revealed that its body waveform (i.e. curvature) during swimming enables the sandfish to operate at maximal undulation efficiency (Maladen et al., 2011b) while expending minimal work (Sharpe et al., 2013). This indicated that the waveform selected was a target of control, or a 'template' (Full and Koditschek, 1999), which muscle activation experimentation confirmed (Sharpe et al., 2013). Furthermore, RFT was successfully used to make predictions of neuromechanical activation patterns during swimming (Ding et al., 2013). This was a consequence of the simplicity of the sandfish shape and body wave, the lack of inertial and non-local effects, and the dominance of environmental forces relative to internal forces.

Compared with other subarenaceous animals that move primarily in dry sand, the sandfish has a relatively small 'elongation ratio' of $L/w=7$, which we define as the ratio of L , the effective body length (effective length accounts for tail tapering, see Materials and methods), to w , the average body width; see examples in Table 1. Other dry-sand subarenaceous squamates exhibit larger elongation, with *Neelaps bimaculatus* having $L/w\approx 50$. Elongation of the body among sand and soil burrowers has been hypothesized to enhance subsurface locomotion performance and possibly energy efficiency (Gans, 1975; Lee, 1998).

In this study, we used the tools described above to test this hypothesis, in particular to study the effects of elongation ratio on sand swimming performance. We did so by performing the first quantitative exploration of the kinematics of locomotion of the shovel-nosed snake, *Chionactis occipitalis* (Hallowell) (Fig. 1A), a desert-

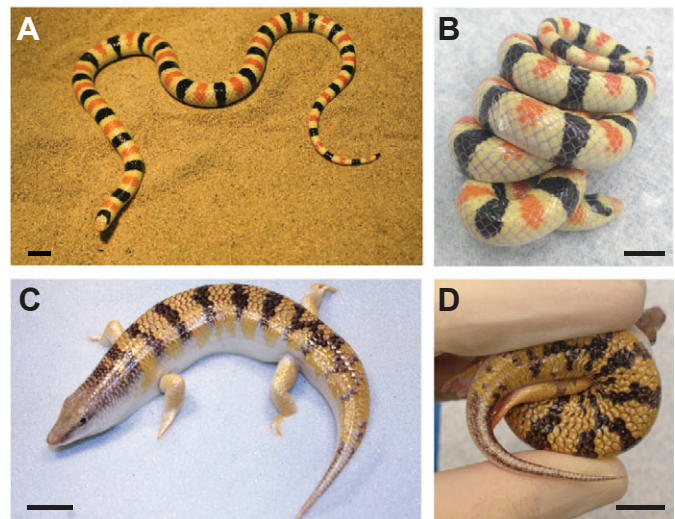


Fig. 1. Subarenaceous animals with different body morphologies.

(A) The long slender shovel-nosed snake (*Chionactis occipitalis*) on sand. Photo credit: Perrin Schiebel. (B) Photograph of an anesthetized snake that can achieve a large number of coils along its body. (C) The sandfish lizard (*Scincus scincus*) resting on 0.3 mm diameter glass particles. (D) Photograph illustrating maximal sandfish bending when applying a slight force along the body. The animal shown is anesthetized. Scale bars in A–D are 1 cm.

dwelling snake whose $L/w\approx 30$ is typical of subarenaceous swimmers. We then used RFT to demonstrate the advantages gained by being long and slender particularly in terms of the efficiency of movement and mechanical cost of transport. RFT allows us to decouple and independently examine the effects of kinematics, body shape and skin–grain friction on sand–swimming performance, all of which could impact locomotion. Therefore, RFT enables us to investigate the extent to which body elongation plays a role. While the sandfish and shovel-nosed snake are evolutionarily constrained by different bauplans (i.e. have divergent body forms and skin properties), our results demonstrate that they have achieved optimized (but not convergent) movement patterns for subarenaceous locomotion.

RESULTS

Morphological and kinematic measurements

Morphological measurements were made on four anesthetized shovel-nosed snakes and 11 anesthetized sandfish. Sandfish have 26

Table 1. Average length to width ratio for subarenaceous squamates

Species name	L/w
Lizards	
<i>Angolosaaurus skoogi</i>	5
<i>Scincus mitranis</i>	7
<i>Scincus scincus</i> *	7
<i>Eremiascincus richardsonii</i>	11
<i>Ophiomorus tridactylus</i>	14
<i>Chalcides mauritanicus</i>	19
<i>Lerista planiventris</i>	20
<i>Neoseps Reynoldsi</i>	20
<i>Sphenops sepsoides</i>	26
Snakes	
<i>Chilomeniscus stramineus</i>	23
<i>Chionactis occipitalis</i> *	33
<i>Neelaps bimaculatus</i>	55

L/w estimated using publicly accessible photographs.

* L/w measured on anesthetized animals.

Table 2. Mean (\pm s.d.) kinematic parameters

Measured parameters	Symbol	<i>Chionactis occipitalis</i>	<i>Scincus scincus</i>	P-value
Elongation ratio	L/w	33.3 \pm 2.5	7.0 \pm 0.4	$P<0.01$
Winding number	W	6.2 \pm 0.8	1.4 \pm 0.06	$P<0.01$
Ventral-forward body-particle friction	μ_s	0.11 \pm 0.02	0.19 \pm 0.02	$P<0.01$
Relative curvature	$\kappa\lambda_s$	6.1 \pm 1.3	7.4 \pm 1.0	$P<0.01$
Undulation number	ξ	3.5 \pm 0.7	1 \pm 0.1	$P<0.01$
Mean slip angle (deg)	β_s	6.4 \pm 1.4	21.3 \pm 4.1	$P<0.01$

presacral (trunk) vertebrae and well-developed limbs (Sharpe et al., 2013), whereas shovel-nosed snakes are limbless and have a variable number of precaudal vertebrae (range 165–175), with our animals representing a population near Yuma, AZ, USA (Cross, 1979). Importantly, with respect to the independent convergence on an elongate and limbless morphology and burrowing ecology highlighted by Wiens et al. (Wiens et al., 2006), our comparison here involves two species that swim through sand, but do so with decidedly different morphologies.

An effective body length was defined for both animals to account for tail tapering (see Materials and methods). L/w for the snake was ~ 5 times larger than that for the sandfish (33.3 \pm 2.5 and 7.0 \pm 0.4, respectively, $F_{1,13}=1348$, $P<0.01$, Table 2). The winding number (W) is defined as the number of coils an animal can form along its body when maximally bent and is equivalent to $W=(\kappa_{\max}/L)/2\pi$, where κ_{\max} is the maximum bending curvature. We measured W on anesthetized animals (three snakes and three sandfish) to bound the maximum number of waves attainable for a given curvature (Fig. 1B,D). The average winding number was larger for the snakes than for the sandfish, $W=6.2\pm 0.8$ and $W=1.4\pm 0.06$, respectively ($F_{1,4}=114$, $P<0.01$). Snake body-particle friction (see Materials and methods for experimental details) was $\sim 50\%$ lower than sandfish body-particle friction on the ventral surface (forward direction: snake $\mu_s=0.11\pm 0.02$, sandfish $\mu_s=0.19\pm 0.02$, $F_{1,4}=29.6$, $P<0.01$; backward direction: snake $\mu_s=0.14\pm 0.02$, sandfish $\mu_s=0.28\pm 0.03$, $F_{1,4,1}=61.9$, $P<0.01$; Tables 2 and 3). However, body friction was similar for the dorsal surface of the snake and the sandfish (forward direction: snake $\mu_s=0.16\pm 0.03$, sandfish $\mu_s=0.18\pm 0.03$, $F_{1,4}=0.6$, $P=0.48$; backward direction: snake $\mu_s=0.24\pm 0.03$, sandfish $\mu_s=0.23\pm 0.02$, $F_{1,4,1}=0.04$, $P=0.85$; Table 3).

Kinematics during swimming

We used a fluidized bed (see Materials and methods and Fig. 7A) to prepare the granular medium into a loosely or closely packed state (LP or CP). [Note that as kinematics were statistically similar (see

supplementary material Table S1) during swimming in these different states, we will report the combined LP and CP averages.] After a gate separating the snake from the granular media was lifted, snakes moved from the rigid surface of the holding container and buried into the prepared sand; during the initial stages of burial, part of the body was in contact with the holding container (Fig. 2A). Snakes buried themselves using an approximately serpenoid waveform with lateral body undulations that propagated from head to tail (Fig. 2B, Fig. 3A; supplementary material Movie 1). During subsurface sand swimming, X-ray imaging revealed that a wave of curvature propagated down the body at 3.7 \pm 1.3 cm s $^{-1}$, 10 times slower than sandfish swimming in which waves of curvature propagated at 39.5 \pm 15.9 cm s $^{-1}$. We estimated the angle of entry of the snakes (the average downward angle of the body relative to the horizontal) using the known arc length between markers and the measured projected distance between markers acquired in the top-view X-ray. We found that snakes moved into media at an entry angle of 23 \pm 10 deg. This value was similar to the angle of entry found for the sandfish (Sharpe et al., 2013).

On initial observation, the shovel-nosed snake appeared to employ a different locomotion strategy from the sandfish – that of tube following, similar to the nematode worm *Caenorhabditis elegans* on an agar surface in which a groove is formed and the material does not yield around the body (Berri et al., 2009). However, when comparing the animal's midline position over a few undulation cycles (Fig. 3A), it was evident the snake did not move in a perfect tube. Previously, we quantified such 'slip' using a measure called the wave efficiency, the ratio of the forward speed to the wave speed (Maladen et al., 2009). This measure assumes that wave speed is constant, the animal's body curvature does not change, and the animal moves forward, on average, along a linear trajectory. Because the snakes often turned during sand swimming such that the body shape was more complicated than a constant amplitude (and direction) wave, we defined a new parameter called the local slip angle, β_s , which is a measurement of the angle between

Table 3. Snake and sandfish skin friction tests

Animal	STL (cm)	SVL (cm)	Mass (g)	μ_s			
				Ventral forward	Ventral backward	Dorsal forward	Dorsal backward
<i>C. occipitalis</i>							
1	33.7		15	0.123 \pm 0.006*	0.142 \pm 0.005*	0.179 \pm 0.003*	0.247 \pm 0.016**
2	38.7		20	0.112 \pm 0.01	0.117 \pm 0.003*	0.177 \pm 0.003*	0.208 \pm 0.006
3	41.4		22.9	0.092 \pm 0.017	0.152 \pm 0.009	0.127 \pm 0.017	0.254 \pm 0.023
Mean (\pm s.d.)				0.109 \pm 0.016	0.137 \pm 0.018	0.161 \pm 0.029	0.236 \pm 0.025
<i>S. scincus</i>							
6	15.4	9.9	24.5	0.201 \pm 0.014	0.271 \pm 0.036	0.208 \pm 0.017	0.254 \pm 0.022
9	14.6	8.8	16.1	0.17 \pm 0.02	0.266 \pm 0.009	0.147 \pm 0.009	0.224 \pm 0.042
11	14	8.5	18.5	0.212 \pm 0.015	0.313 \pm 0.04	0.183 \pm 0.014	0.217 \pm 0.017
Mean (\pm s.d.)				0.194 \pm 0.022	0.283 \pm 0.026	0.179 \pm 0.031	0.231 \pm 0.019

STL, snout-tail length; SVL, snout-vent length; μ_s , body-particle friction (μ_s data are means \pm s.d.). Length and mass reflect measurements made on the day of the friction experiments.

$N=4$ measurements unless marked otherwise: * $N=3$ measurements, ** $N=2$ measurements.

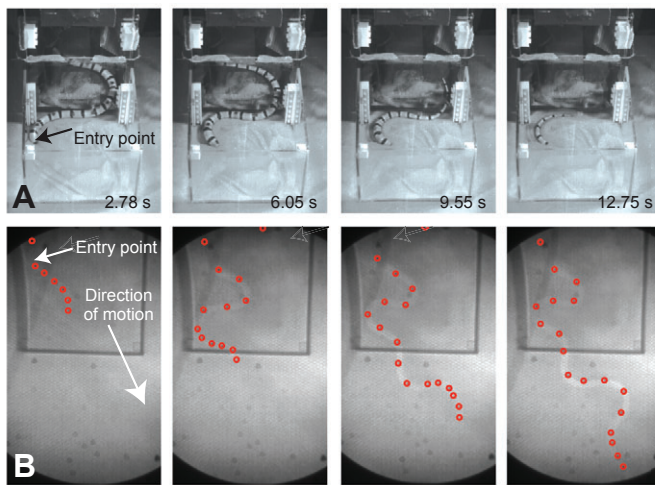


Fig. 2. A shovel-nosed snake burrowing into granular media. Sequence showing (A) above-surface and (B) X-ray images of the shovel-nosed snake during burial into granular media (0.3 mm diameter glass particles) measured from the start of burial ($t=0$ s). Red circles in B show the marker positions along the body (markers 1–6 are spaced at 1 cm intervals and markers 7–20 are spaced at 2 cm intervals) that were used for B-spline reconstruction of the body midline during burial. The estimated entry angle (relative to the horizontal) for this trial is 25 deg.

the direction of movement of a body segment and the body segment orientation. We measured this parameter at every marker along the body during subsurface movement using the relationship $\beta_s = \cos^{-1}(|\hat{v}_{t,m} \cdot \hat{T}_{t,m}|)$, where \hat{v} is the unit velocity vector and \hat{T} is the tangent vector at a body marker location (m) and time (t). Physically, this quantitatively measures the local deviation from ‘tube’ movement.

The slip measurements depend on the accuracy of the vector calculations. To determine body midline positions and tangent vector directions in the presence of relatively large detector noise (occlusions from above-surface chamber walls, and movement of the granular media), we developed a marker detection and tracking strategy that provided the trajectories of multiple markers to sub-pixel accuracy. We used a recursive Bayesian approach to marker trajectory estimation with linear models and Gaussian noise, leading to a combined Kuhn–Munkres algorithm and Kalman filtering formulation. The inclusion of a B-spline model for predicting the subject’s movement provided additional robustness to image artifacts and unobservable markers. For details, see Materials and methods and supplementary material Movie 1 (M.S., S.S.S., D.I.G. and P.A.V., in preparation).

We define the spatial and temporal average of the slip angle as $\bar{\beta}_s$; the average is computed over all markers visible during a trial. The markers, m , over which β_s was averaged varied depending on marker visibility, but we always excluded the first and last marker, which were more susceptible to error due to the B-spline fitting error at the end points. $\bar{\beta}_s$ is inversely related to the wave efficiency for a sinusoidal straight swimmer, but is more general because it can be calculated for animals that move along any arbitrary path, change undulation frequency, or change shape during movement.

$\bar{\beta}_s$ was measured for snake swimming (three snakes, 18 trials) and sandfish swimming (six sandfish, 56 trials). Angular differences between velocity and tangent vectors at the tracked marker positions (Fig. 3C,D) varied along the body and during time for both animals but were larger during sandfish subsurface locomotion compared with snake locomotion, resulting in high local slip (β_s)

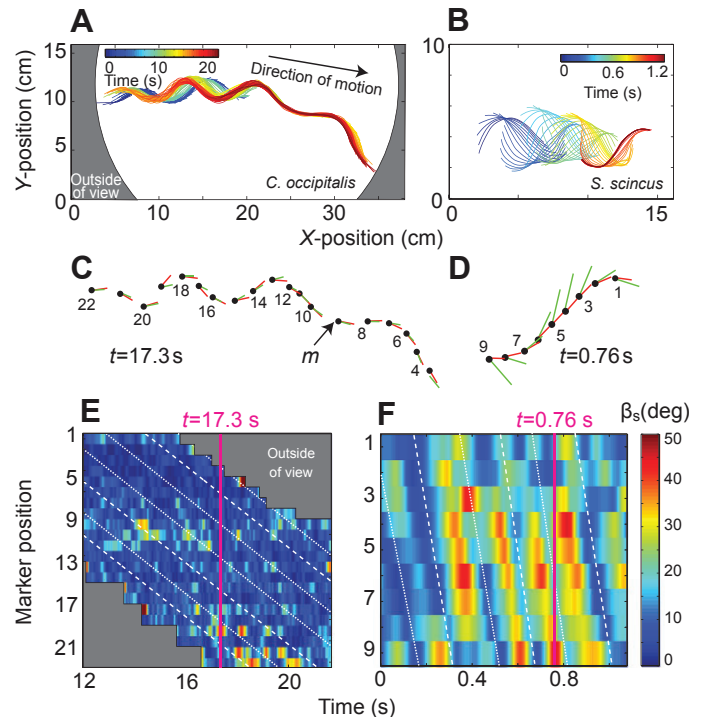


Fig. 3. Slip comparison between the shovel-nosed snake and the sandfish. (A) Shovel-nosed snake midline position during subsurface locomotion. Different time instances are shown with color; time $t=0$ is shown in dark blue and $t=23$ s is shown in dark red. The body midlines are plotted in 0.17 s time increments (note that the snake paused in this trial between 4 and 10 s). Gray regions are beyond the field of view. (B) Sandfish body midline during subsurface swimming at different time instants, where time $t=0$ is dark blue and $t=1.2$ s is dark red. A body midline is plotted every 0.02 s. Markers along the sandfish body extend from 0.3 snout–vent length (SVL) to 1.1 SVL and are shown by colored curves. (C,D) Velocity vectors (green) and tangent vectors (red) at markers, m , along the snake body (C) and sandfish body (D) are shown for a single time instant during subsurface movement for two representative trials. m increases from head to tail. (E,F) Images show local slip angles (β_s) during snake swimming (E) and sandfish swimming (F). Data have been low-pass filtered with a first-order Butterworth filter. White dotted and dashed lines show when curvature is 0 along the body; curvature propagates from head to tail with increasing time. Dashed-to-dashed (or dotted-to-dotted) lines show 1 undulation cycle. The dark gray solid region indicates when markers were outside of the field of view and slip was not measured. Pink lines in E and F correspond to the time instant shown in C and D, respectively. The first marker and last marker were excluded from the averages because of error in the B-spline fit associated with the end-points (see the Materials and methods).

measurements (see Fig. 3E,F, for β_s during a representative snake and sandfish trial, respectively). Thus, the average slip angle $\bar{\beta}_s$ for snake sand swimming was small ($\bar{\beta}_s=6.4\pm 1.4$) compared with sandfish sand swimming ($\bar{\beta}_s=21.3\pm 4.1$, ANOVA, $F_{2,73}=280$, $P<0.01$).

Previous work suggested that the sandfish wave efficiency (and therefore slip) depended on kinematic variables (Maladen et al., 2011b) such as maximum curvature and undulation number. Therefore, we next examined differences in kinematics between the snake and sandfish by measuring the relative curvature and number of waves along the body during sand swimming for each. We measured the maximum local curvature, κ_{\max} , using a best fit circle to each bend and measured the half-arc length, $\lambda_{s/2}$, determined as the length between locations of zero curvature, for each bend (see Fig. 4A); here s denotes arc length. The relative curvature, κ/λ_s ,

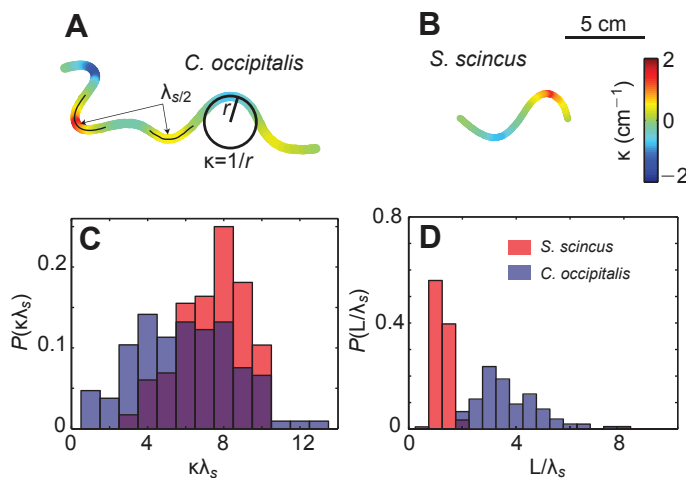


Fig. 4. Distribution of local relative curvature and local undulation number for the snake and sandfish trials. (A,B) Signed curvature κ is shown along a representative snake (A) and sandfish body (B) at an instance during swimming. To reduce error, the maximum local κ was determined by fitting a circle to each bend, and calculating $\kappa=1/r$ using the resulting radius of the circle, r . The arc length for each half-wave, $\lambda_{s/2}$, was found by measuring the distance along the body starting with a location of zero curvature to the next location of zero curvature. Note: only the portion of the snake that is subsurface and within the field of view is shown in A. (C) Probability distribution of local relative curvature $\kappa\lambda_s$ for all snake (blue) and sandfish (red) trials. (D) Probability distribution of the local undulation number (the effective body length divided by twice the arc-wavelength of a bend, L/λ_s). Effective body length was measured prior to experimentation on anesthetized animals. $\lambda_{s/2}$ was determined from video analysis and scaled to account for the entry angle. For the sandfish, all trials were scaled to account for the average entry angle of 23 deg (see Sharpe et al., 2012); for the snake, each trial was scaled by the entry angle estimated for each run using known distances between markers and projected distances.

determined as $2\kappa\lambda_{s/2}$ of each bend along the body, was calculated for each snake and sandfish trial at an instant in time when most (if not all) of the animal was within the field of view and for submerged body portions only. $\kappa\lambda_s$ did not vary with media compaction for either animal. Snakes had a broader distribution of $\kappa\lambda_s$ during swimming compared with sandfish, where $\kappa\lambda_s$ of each bend along the body was considered an independent measurement (Fig. 4C). The mean $\kappa\lambda_s$ ($\overline{\kappa\lambda_s}$) for a single trial was calculated by averaging $\kappa\lambda_s$ over all bends visible along the body.

On average, snake trials had a slightly but significantly lower $\overline{\kappa\lambda_s}$ than sandfish trials ($\overline{\kappa\lambda_s}=6.1\pm 1.3$ for snakes, and $\overline{\kappa\lambda_s}=7.4\pm 1.0$ for sandfish; ANOVA, $F_{2,73}=20.3$, $P<0.01$; Table 2). Because the snake was more inclined to turn during movement, we compared the distribution of $\kappa\lambda_s$ for straight swimming trials, in which the snake was moving on average along a straight trajectory, and for all swimming trials, in which the snake may turn or move straight (see supplementary material Fig. S2). Both sets of trials showed a broad distribution of $\kappa\lambda_s$, indicating that snakes employ small and large $\kappa\lambda_s$ even during straight undulation cycles. Furthermore, we found the curvature along each bend decreased as the snake moved farther (and therefore deeper) into the media (ANOVA, $F_{7,105}=3.3$, $P<0.01$ for all trials considered), but this trend was more pronounced when considering straight swimming alone. For straight swimming, the maximum $\kappa\lambda_s$ decreased as the snake moved deeper into the medium (see Materials and methods and supplementary material Fig. S2).

The snake also swam with a higher number of waves along its body; we refer to this quantity as the undulation number, ξ ,

determined from counting the waves on the animal's body at an instant in time when all or most of the body was within the field of view (see Materials and methods for more details). The mean undulation number across all trials, $\overline{\xi}$, was larger for the snake ($\overline{\xi}=3.5\pm 0.7$) than for the sandfish ($\overline{\xi}=1\pm 0.1$, ANOVA, $F_{2,73}=695$, $P<0.01$) and did not statistically vary with granular media compaction for either animal (Table 2). As both wave curvature and wavelength changes along the body, we explored local characteristics by calculating a related measure called local undulation number, defined as the ratio of effective body length to twice the arc length of each body bend (or half wave), L/λ_s ; if λ_s is constant along the body, then $L/\lambda_s=\overline{\xi}$. Similar to ξ , the distribution of L/λ_s for the snake was wider and the average was larger than that of the sandfish (Fig. 4D).

RFT calculations of slip

The low slip locomotion of the snake appears 'efficient' compared with that of the sandfish. However, it is unclear whether these kinematic differences are due to lower skin friction, the larger number of waves propagated along the body during swimming, the snake's more slender body, or some combination of these factors. Inspired by our observation that the slip is finite and thus material yields in a small region around the body, we next applied the granular RFT (discussed in Materials and methods) to the snake to tease apart the effect of these factors on subarenaceous movement. In the model, we assumed that the animal targeted a particular kinematic traveling wave pattern, thereby applying a neural control strategy to bend its body into a desired shape; we will return to this point later in the paper. To calculate slip on such a deforming shape, we generated waves of constant curvature, wavelength and undulation number, and simulated horizontal plane swimming at a depth of 7.6 cm (see Materials and methods). We modeled swimming for two different body morphologies: one with elongation ratio $L/w=7.1$ (similar to the sandfish) and another with $L/w=33.5$ (similar to the snake), but with the same coefficient of body-particle friction, $\mu_s=0.17$. Note that both turning and straight (i.e. average midline follows a straight path) snake experimental swimming trials were considered in our analyses. Analysis of all trials was supported by theory, which revealed that simulation of a swimmer moving in a circle with a given average $\kappa\lambda_s$ yielded similar β_s values to those for straight swimming.

The theory predicted that increasing curvature resulted in decreased slip, β_s (Fig. 5). Using a larger undulation number ($\overline{\xi}$) also decreased β_s but yielded diminishing returns for $\overline{\xi}>2$. Despite the reduction in slip due to the long, slender body, the RFT calculations did not match the observed slip values for the snake. However, because the snake's ventral skin-grain friction was approximately half that of the sandfish, we next decreased friction in the RFT simulations by reducing tangential drag forces by 50% (see supplementary material Fig. S1) (Fig. 5, dashed curves). Theory predicted a greater than 50% decrease in β_s , and thus fell within the experimentally observed slip range for the snake when considering its kinematics.

Our previous work demonstrated that the sandfish targeted optimal kinematics to maximize undulatory efficiency (η_u , forward distance moved per cycle normalized by λ_s) and minimize the mechanical cost of transport (CoT, sum of the power to external surroundings, normalized by body weight and speed, neglecting internal forces) (Sharpe et al., 2013). These results suggested that intermediate curvature waves can be a control target for optimal sand swimming and could therefore be a 'template' for subarenaceous locomotion. In accord with the optimal swimming hypothesis, we found that the snakes also operated within a $\overline{\kappa\lambda_s}$ and $\overline{\xi}$ range that is optimal (Fig. 6A,B). As with previous work exploring sandfish

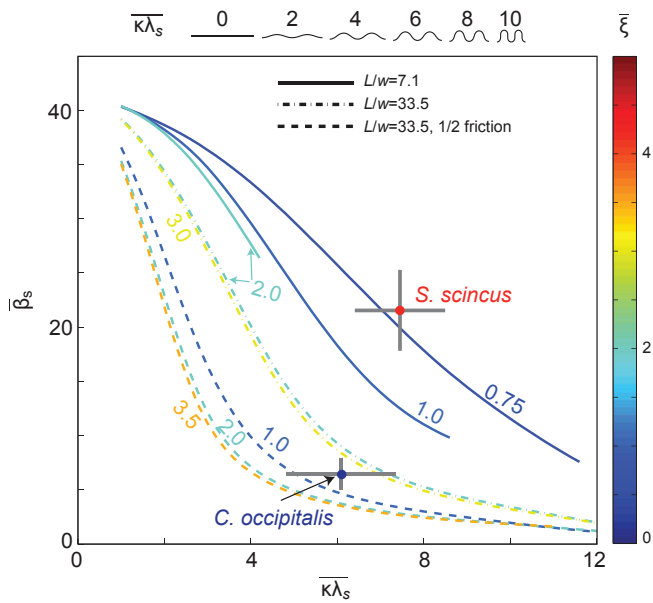


Fig. 5. Granular resistive force theory (RFT) predictions of mean slip angle (β_s) with changing mean relative curvature ($\overline{\kappa\lambda_s}$), average number of undulations along the body ($\overline{\xi}$), body length to width ratio (L/w) and effective friction. Force relationships were established from empirical drag data in loosely packed (LP) media. The color of the curves and experimental data correspond to different $\overline{\xi}$ (where dark blue is $\overline{\xi}=0$, dark red is $\overline{\xi}=5$). Solid curves are predictions for an undulatory swimmer with a $L/w=7.1$ and body–particle friction, μ_s , of 0.17. The dotted-dashed curves show the theoretical predictions with $L/w=33.5$ and μ_s of 0.17. The dashed curves are the predictions for $L/w=33.5$ and half the tangential force (which occurs when there is a 50% decrease in body–particle friction, i.e. μ_s of 0.085; see supplementary material Fig. S1). Experimental data are shown for sandfish (gray cross with red center) and snake (gray cross with blue center) trials in CP and LP media. Horizontal and vertical lines are centered on $\overline{\kappa\lambda_s}$ and $\overline{\beta_s}$, respectively, with span representing ± 1 s.d. The diagram above the main panel illustrates waves with different $\overline{\kappa\lambda_s}$.

swimming efficiency (Maladen et al., 2009), there is a slight difference between undulation efficiency in LP and CP media. There is a larger difference in CoT; swimming in LP requires approximately half the power. However, the minimum CoT occurs when using similar $\overline{\kappa\lambda_s}$ for both CP and LP simulations. Accordingly, we found statistically similar CP and LP experimental kinematics for both sandfish and snakes (see supplementary material Table S1 for separated CP and LP values). We note that simplifications necessary in modeling and/or physiological pressures could account for the slight difference between experimentally observed kinematics and the model-predicted optimal kinematics.

DISCUSSION

Experiments revealed that the snake swam in a frictional fluid with a lower average slip angle than the sandfish. Granular RFT captures this performance differential and revealed at least two locomotor benefits of having a long, slender body. (1) For a given curvature and undulation number, a larger elongation ratio yields a slightly smaller slip. This suggests that when using the same kinematics, a more slender and/or longer body will yield lower slip locomotion. However, the change in slip is small and cannot account for the large decrease observed between the sandfish and snake. (2) A larger winding number (a consequence of possessing a larger L/w and a greater number of vertebral segments) allows an undulatory swimmer to increase its undulation number while maintaining a high average curvature; therefore, animals with a larger elongation ratio

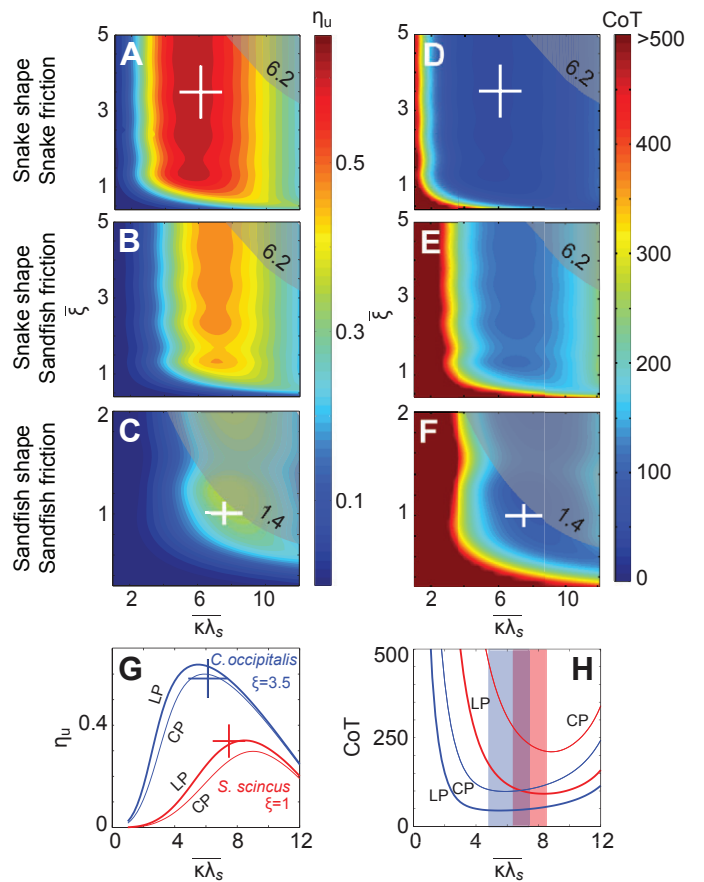


Fig. 6. Granular RFT predictions of undulation efficiency (η_u), the distance traveled per cycle normalized by λ_s (the arc length between successive bends) and mechanical cost of transport (CoT) at experimentally determined $\overline{\xi}$. For these simulations, swimmers undulate within a horizontal plane at a depth of 7.62 cm. (A–C) Undulation efficiency η_u and (D–F) weight-specific mechanical CoT during swimming in LP media as a function of $\overline{\xi}$ and mean relative curvature ($\overline{\kappa\lambda_s}$) for $L/w=33.5$, 1/2 friction (A,D); $L/w=33.5$, sandfish friction (B,E); and $L/w=7.1$, sandfish friction (C,F), where $L/w=33.5$ corresponds to snake shape and $L/w=7.1$ corresponds to the sandfish shape, dark red is an undulation efficiency η_u of 0.65 and dark blue is $\eta_u=0$. The white bars show the mean and s.d. of experimentally determined $\overline{\xi}$ and $\overline{\kappa\lambda_s}$ for the snake (A,D) and sandfish (C,F). The gray region indicates the area that the animals cannot access because of their winding number, which limits $\overline{\xi}$ and $\overline{\kappa\lambda_s}$. (G) Undulation efficiency η_u and (H) CoT versus relative curvature are shown for the snake (blue) and sandfish (red) at $\overline{\xi}=3.5$ and $\overline{\xi}=1$, respectively. The thick curves are theoretical predictions for swimming in LP media and the thin curves are for CP media. In G, the blue and red crosses show the mean and s.d. of the experimentally determined undulation efficiency (vertical lines) and relative curvature (horizontal lines) for the snake and sandfish, respectively, for combined CP and LP trials (see supplementary material Table S1 for separated values). In H, shaded bars show the $\overline{\kappa\lambda_s}$ range that the sandfish (red) and snake (blue) operate at in all trials.

(and an increased number of vertebrae) can utilize a greater range of curvatures and undulation numbers. In contrast, an animal with a low winding number may have to decrease curvature to achieve a higher undulation number and vice versa. For example, for the sandfish’s body shape ($L/w=7.1$) and winding number ($W=1.4$), if $\overline{\xi}=2$ the swimmer is constrained to operate with $\overline{\kappa\lambda_s}<4.3$ (Fig. 5, solid cyan curve). Therefore, it is more advantageous for a swimmer with a low elongation ratio to utilize a smaller number of waves along its body, which enables high curvature swimming kinematics. However, for the slender snake, this compromise is not necessary (Fig. 5, see dotted-dashed cyan curve).

Our results also imply that the longer body and lower friction allows the snake to achieve a higher undulation efficiency and lower mechanical CoT than possible for a sandfish given its bauplan (Fig. 6). We postulate that the bauplan exemplified by the shovel-nosed snake may also approach that of an optimal sand swimmer. While a longer body with a greater number of vertebrae would allow the animal to utilize a higher undulation number or relative curvature, RFT calculations show diminishing returns in undulation efficiency (Fig. 5 and Fig. 6A). In addition, a longer body would also incur greater frictional drag, and thereby increase CoT. Further systematic exploration of the RFT model is needed to test this idea.

Our results suggest how low skin friction offers a biomechanical advantage for sand swimming and support prior statements that smooth skin is an adaptation that is characteristic of subterranean animals (Mosauer, 1932). However, more quantitative studies that measure skin friction using the same technique and on a multitude of species, both fossorial and non-fossorial, are needed to support this claim. And while RFT predicts that lower friction would improve performance, the shovel-nosed snake skin friction ($\mu_s \approx 0.11$ on the ventral surface) may be one of the lowest found for squamates in nature (Berthé et al., 2009; Gray and Lissmann, 1950; Hu et al., 2009) and additional reductions could be morphologically constrained.

Somatic elongation has evolved independently many times among squamate reptiles, involving all snakes and multiple examples among the ‘lizards’ (i.e. non-snake squamates) (reviewed by Wiens and Slingluff, 2001). Elongation has been achieved differentially by elongation of the trunk and/or the tail, and typically includes reduction or loss of the limbs. Burrowing ecology has been associated with elongation in squamates, but many elongate taxa do not burrow. The burrowing bauplan typically includes elongation of the trunk with a relatively short tail (Wiens et al., 2006), and this association holds for the shape of the shovel-nosed snake. Thus, the convergence of a long trunk (via an increased number of precaudal vertebrae), relatively short tail and reduction/loss of limbs in association with burrowing is a well-established repeated theme in the evolution of squamates (Brandley et al., 2008; Sites et al., 2011). Our comparison here focused on two species that have converged ecologically on a subarenaceous burrowing lifestyle, yet unlike typical evolutionary comparisons (e.g. Wiens et al., 2006) the sandfish and shovel-nosed snake are not convergent in morphology. The shovel-nosed snake is a typical serpent, albeit with a relatively short tail, while the sandfish is a typical limbed lizard that is phylogenetically nested in a clade that does not include elongation or limblessness (Wiens et al., 2006). Furthermore, the sandfish lizard uses its limbs during initial burial to achieve rapid submergence and during foraging activities. Our comparisons reveal evident patterns of performance optimization and constraint based on two remarkably different squamate body forms. Furthermore, this study reveals the functional benefits of elongation on burrowing locomotion, providing the first quantitative support for the hypotheses made by Gans (Gans, 1975) that elongation leads to enhanced subsurface locomotor performance and decreases energy expenditure, and provides a functional link between correlations noted between burrowers and adaptive body features (Lee, 1998).

Conclusions

We used X-ray imaging to reveal the kinematics of sand swimming of the shovel-nosed snake, and then used a granular RFT to quantitatively determine how the snake’s body morphology and skin friction conspire to achieve high performance. Our model reveals that a long, slender, slick (and limbless) (Lee, 1998; Wilson, 2012)

body leads to high swimming performance in subarenaceous animals – the snake’s long body and high winding number allow it to operate over a wide range of curvatures and wave numbers. Both subarenaceous animals in this study swim with a body wave curvature that maximizes undulatory efficiency and minimizes the mechanical CoT for their particular bauplans. This provides evidence that both animals target these kinematics, supporting the idea that control for such waveforms is a ‘template’ for sand swimming.

More broadly, sand swimming continues to be an excellent system for making detailed comparison between experiment and theory in a locomoting biological system. In this non-inertial, friction-dominated environment, internal body forces are small compared with environmental forces (Ding et al., 2013), and shape changes determine locomotor efficacy. Combined with the relative simplicity of the granular frictional fluid environment, the system allows the teasing apart of relative contributions of shape, friction, wave properties and even aspects of neuromechanical control (Ding et al., 2013). Such tools might also prove useful to address questions in functional morphology and ecologically driven adaptation (Garland and Losos, 1994) in dry granular media (e.g. cranial modifications, smooth skin and miniaturization) that occur in a diversity of burrowing reptiles (Gans, 1975; Lee, 1998; Mosauer, 1932; Rieppel, 1988; Wiens and Slingluff, 2001; Wilson, 2012).

MATERIALS AND METHODS

Shovel-nosed snakes are found in the Mojave and Sonoran deserts, typically near dry sand dunes (Norris and Kavanau, 1966). The shovel-nosed snake moves only short distances on the surface of sand, in comparison with other snakes, and readily buries into granular media (Mosauer, 1932; Mosauer, 1933; Mosauer, 1936; Norris and Kavanau, 1966) to depths of 60 cm beneath the ground (Cowles, 1941). *Chionactis occipitalis* were collected in accordance with a scientific collection permit (no. SP591773) approved by the Arizona Game and Fish Department. All snake experiments were conducted under the Georgia Institute of Technology IACUC protocol A11066.

Sandfish lizards, *Scincus scincus*, were purchased from commercial vendors (LLL Reptile, Vista, CA, USA and Ocean Pro Aquatics, Chino Hills, CA, USA). Data sets were analyzed from previous work (see Sharpe et al., 2013). All experimental procedures were conducted in accordance with the Georgia Institute of Technology IACUC protocol number (A08012) and Radiation Safety protocol (X-272).

Morphology and skin friction

Morphological measurements were made on four anesthetized snakes and 11 anesthetized sandfish (Table 4). Both animals were sedated by 5% isoflurane gas induction and then anesthetized with an intramuscular injection of ketamine hydrochloride (200 mg/kg body mass). We report average masses and lengths for animals that were measured more than once over the course of the study.

SVL, STL, w and mass were recorded for each animal. Snakes had a consistent body width, $w \approx 1$ cm, and long bodies with an average STL of 36.6 ± 2.8 cm (see Table 4). A noticeable reduction in body diameter occurred between 0.85 and 0.9 STL. Therefore, we defined an effective snake length (L) to account for this tail tapering as $L = 0.87\text{STL}$. On average $L = 31.8 \pm 2.4$ cm for snakes. The sandfish width was $w \approx 1.5$ cm, the STL was on average 14.1 ± 0.9 cm, and the SVL was 8.9 ± 0.5 . We accounted for tail tapering in sandfish by defining L as 1.2SVL , determined from morphological observations, which was on average 10.6 ± 0.6 cm. Snake and sandfish masses were similar (17.5 ± 3.4 and 17.6 ± 2.8 g, respectively). The elongation ratio, L/w , was calculated using the effective length and body width measurements. L/w for the snake was ~ 5 times larger than that for the sandfish (33.3 ± 2.5 and 7.0 ± 0.4 , respectively).

Morphological measurements were also made on awake animals used in kinematic experiments on the day of data collection. Because awake animals

Table 4. Snake and sandfish morphology

Animal	SVL (cm)	STL (cm)	L (cm)	w (cm)	Mass (g)	L/w
<i>C. occipitalis</i>						
1		32.5	28.3	0.95	12.6	29.8
2		38.7	33.7	0.95	20	35.5
3		37.5	32.6	0.97	19.4	33.5
4		37.5	32.6	0.95	18	34.3
Mean ± s.d.		36.6±2.8	31.8±2.4	0.96±0.01	17.5±3.4	33.3±2.5
<i>S. scincus</i>						
1	8.7	14.2	10.4	1.5	16	6.9
2	9	14.0	10.8	1.4	18.8	7.7
3	9	12.5	10.8	1.7	19	6.4
4	8.3	13.6	10.0	1.4	15.8	7.1
5	8.8	14	10.6	1.4	14.5	7.5
6	10.0	15.7	12.0	1.7	24.1	7.1
7	9.1	15.1	10.9	1.6	18.1	6.8
8	8.3	13.4	10.0	1.5	14.2	6.7
9	8.8	14.4	10.5	1.5	16	7
10	9	14.6	10.8	1.6	18.1	6.8
11	8.5	14	10.2	1.5	18.5	6.8
Mean ± s.d.	8.9±0.5	14.1±0.9	10.6±0.6	1.5±0.1	17.6±2.8	7.0±0.4

tended to bend their bodies and move during measurements, the measurements were subject to more error in accuracy. However, average L/w values were similar for these animals to those made on the anesthetized animals (35.6 ± 3.4 for the snakes, $N=3$ animals, and $L/w=7.3 \pm 0.2$ for sandfish, $N=6$ animals).

Winding number (W) was measured by bending the bodies of three anesthetized snakes and three anesthetized sandfish lizards. Bodies were maximally bent to determine the total number of coils that could be formed along the body from the snout tip to the effective body length. W was used to determine the maximum relative curvature that the animal could attain given a serpentine waveform and fixed number of waves along the body.

Body-particle friction measurements were made using 0.3 mm glass particles (the experimental media) following techniques described elsewhere (Hu et al., 2009) (Fig. 7B). Animals were placed on an inclined plane covered with a monolayer of particles such that either their ventral or their dorsal surface was in contact with the particles. Their head was either oriented downward (causing 'forward' sliding) or upward (causing

'backward' sliding) relative to the sloping angle. In total, four orientations were tested. The edge of the plane was lifted until an inclination angle (θ_{slide}) was reached that caused animals to slide (Fig. 7B). The static coefficient of friction, μ_s , was calculated from the relationship $\mu_s = \tan(\theta_{\text{slide}})$. An anesthetized animal was placed on the monolayer of particles adhered to a board. One edge of the board was lifted and θ_{slide} at which animal slid was recorded. Four friction measurements were made in each orientation (unless otherwise noted in Table 3) on three snakes and three sandfish lizards.

Substrate preparation and trial conditions

LP and CP compactions were achieved using a fluidized bed and shaking apparatus similar to prior experimentation (Fig. 7A) (Gravish et al., 2010; Li et al., 2009; Sharpe et al., 2013). The bed ($22.9 \times 40.6 \text{ cm}^2$) was filled with glass particles (diameter = $0.27 \pm 0.04 \text{ mm}$ and density = 2.5 g cm^{-3}) to a height of 10 cm; such particles approximate fine desert sand. The same bed and granular particles were used for both snakes and sandfish kinematic trials, but slightly different shaking apparatuses were used to generate CP states. Consequently, a 2% difference in CP volume fraction (ϕ , measured as the ratio of the volume of the granular medium to the volume of its occupied space) occurred between snake and sandfish experiments, where snake CP trials were at $\phi = 0.617 \pm 0.012$ and sandfish CP trials were at $\phi = 0.635 \pm 0.013$. A LP compaction of $\phi = 0.58$ was achieved for both sandfish and snake experiments. Because compaction did not influence kinematics for either animal (see supplementary material Table S1), the difference in CP states should not affect the results.

Snake experiments took place at an average ambient temperature of 25°C and average humidity level of 41%. Lights heated the granular substrate for $\sim 1 \text{ h}$ prior to experimentation and the temperature of the sand was measured prior to each trial. The average sand temperature for all trials was $32.5 \pm 2.5^\circ\text{C}$. The bed was periodically fluidized, which helped homogenize the distribution of temperatures within the bed, and lights were turned off when necessary to keep a constant sand temperature. A similar setup was used for the sandfish lizard experiments (see Sharpe et al., 2013).

Previous sandfish locomotion studies showed that sandfish kinematics were similar in the two preparations (Maladen et al., 2009; Sharpe et al., 2013). Similar snake kinematics were obtained in LP and CP preparations; therefore, the results reported represent the combined data for the two preparations unless otherwise specified (see supplementary material Table S1 for separated kinematic results for LP and CP trials).

Swimming kinematics

Subsurface kinematics were recorded for three of the snakes (snake nos 1, 3 and 4; see Table 4) and each were tested in three CP and three LP granular media preparations, with a total of 18 snake trials considered in the analysis.

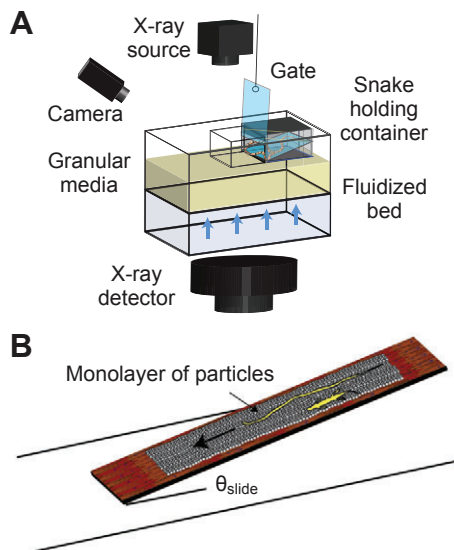


Fig. 7. Experimental apparatus. Diagram of the apparatus used to (A) collect subsurface snake kinematics and (B) measure the coefficient of static friction (μ_s) between the animal's body and granular particles by observing the angle (θ_{slide}) at which the animal begins sliding. The snake and sandfish are shown in the 'forward' direction (as denoted in Table 3).

Kinematic sandfish data were utilized from previous studies (Maladen et al., 2009; Sharpe et al., 2013). Fifty-six undulations were considered from different trials taken across six animals for comparison with snake data. All experimental procedures were conducted in accordance with the Georgia Institute of Technology IACUC protocol nos A11066 and A08012 and radiation safety protocol no. X-272.

Snakes were placed in a container resting above the surface of the prepared sand (Fig. 7A). A gate, separating the snake from the granular media, was lifted and the bottom-rear section of the container was also lifted via a string connection, causing the snake's orientation to angle downward toward the media. Transparent walls resting on the surface of the sand outside the holding container ensured burial at a desired location away from container walls and within the X-ray field of view. Above-surface visible light video was recorded at 63 frames s⁻¹ using a high-speed camera (AOS Technologies AG X-PR1). Subsurface snake kinematics were recorded using an X-ray system (OEC 9000) coupled to a high-speed camera (Fastcam 1024 PCI, Photron). Top-view (i.e. dorsal view) subsurface snake kinematics were recorded at 60 frames s⁻¹. The X-ray system was set to an energy of 85 kV and 20 mA. Because of the apparatus position and X-ray image intensifier size, the field of view within the container was limited to a 20 cm diameter circle; all portions of the snake were not always visible in X-ray images. To enhance contrast, small markers (~1 mm² each, mass ~0.01 g) made from lead were bonded to the midline of the snake using cyanoacrylate glue. These markers were placed at 1 or 2 cm increments down the length of the body. Markers were tracked using custom-written MATLAB code (M.S., S.S.S., D.I.G. and P.A.V., in preparation). If a marker did not exist at every 1 cm location, that location was manually tracked over the course of the trial. A third-order Basis spline (B-spline) was fitted to the snake's body at every frame for all markers visible (see below for more details).

Kinematics were characterized during subsurface movement. The number of undulations along the body, ξ , was determined by counting the waves along the body (to the nearest 0.1 wave) for all animals during a time when most, if not all, of the body was within the field of view. When the full length of the snake was not within the field of view or subsurface, ξ was calculated as $\xi_{\text{inside}} + \xi_{\text{outside}}$. ξ_{inside} was directly counted, while ξ_{outside} was estimated by using the known length of the snake outside of the field of view and the average wave arc length (λ_s). The local undulation number was also characterized and defined as the ratio of the animal's effective length to the local wavelength, L/λ_s . λ_s was found for each bend using X-ray images during sand swimming and measuring the half-wave arc length, $\lambda_{s/2}$, between two adjacent locations of zero curvature and multiplying by 2 (Fig. 4). λ_s was then scaled by the estimated snake entry angle to compare with the effective body length, L . Relative local curvature ($\kappa\lambda_s$) was used for a non-dimensional comparison with the sandfish data and calculated as $2\kappa\lambda_{s/2}$, where κ was determined for each bend using a best fit circle near the maximum. To calculate slip, tangent vectors, \hat{T} , at varying body locations were found by using the tangent to a B-spline that was fitted to the midline position of the snake at every frame (see below). Unit velocity vectors, \hat{v} , were spatially filtered to remove tracking noise. B-splines were also fitted to the sandfish midline during previously recorded trials. Only subsurface kinematics were considered for analyses, where 'subsurface' was defined as when, at minimum, the cloacal opening was covered by granular media. Identical methods to those described for the snake were used to estimate ξ , λ_s , κ and β_s for the sandfish.

Statistics were performed using the software package JMP (SAS Institute, Cary, NC, USA). The results were considered significant if the P -value was smaller than 0.05. Values are shown as means \pm s.d.

RFT calculations

The granular RFT [based on the model introduced in Maladen et al. (Maladen et al., 2009) and illustrated in Fig. 8] used a simplified model of the snake and sandfish kinematics such that $\kappa\lambda_s$ values for all bends along the modeled undulatory swimmer's body were the same and no turning occurred. The modeled animals had a uniform body with a circular cross-section and blunt head, and propagated a serpentine wave from head to tail. Bending stiffness measurements in Ding et al. (Ding et al., 2013) demonstrated that for the sandfish, internal forces were small compared with forces required to move through the medium. Therefore, we also used this assumption for the snake.

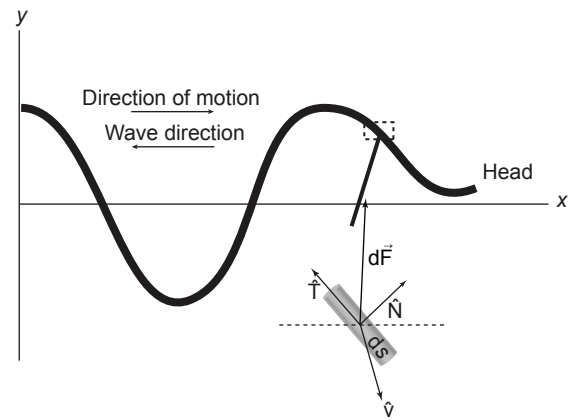


Fig. 8. Schematic illustration of force on a body element associated with a time-dependent shape, modeling the self-deformation of a swimming organism. These forces are used as input into the granular RFT. In the calculations in the Materials and methods for the snake and the sandfish lizard, the wave is of uniform amplitude; see Fig. 5 for examples.

A serpentine wave is described by:

$$\theta(t) = \theta_{\text{max}} \sin \frac{2\pi}{\lambda_s} (s + v_c t), \tag{1}$$

where t is time, s is the distance along the path, θ is the angle between the direction along the wave at position s and the forward direction (Leopold, 1994), θ_{max} is the maximum angle of deviation (or maximum θ) and v_c is the velocity of the curvature wave.

The force distribution along the swimmer's centerline was estimated using the granular RFT. The force distributions used in the granular RFT model are semi-empirical relationships [measured and discussed in Maladen et al. (Maladen et al., 2009; Maladen et al., 2011b)] based on the drag forces on a stainless steel rod submerged to animal movement depths and with a friction coefficient and dimensions similar to those of the sandfish. These forces are assumed to be independent of the speed and increase with the so-called 'lithostatic pressure' $k\rho gz$, with z the depth beneath the free surface, ρ the particle material density and g the gravitational acceleration, and where for loose-packed particles $k \approx 2.5$ and is an empirical constant that depends on particle properties. The lithostatic pressure in a granular medium is analogous to the hydrostatic pressure in fluids and results from an increased load of material for increased depth. For a segment of a cylinder with length ds , radius r and unit velocity \hat{v} relative to the in-plane normal and tangent vectors \hat{N} and \hat{T} the infinitesimal force is:

$$d\vec{F} = 2k\rho g r \langle z \rangle [f(\hat{N} \cdot \hat{v})\hat{N} + (\hat{T} \cdot \hat{v})\hat{T}] ds, \tag{2}$$

where the anisotropy function is given by:

$$f(q) = \left(1 + \frac{C}{\sqrt{\tan^2 \gamma_0 + (q)^2}} \right) q, \tag{3}$$

with empirically determined (and material dependent) constants $C=1.8$ and $\gamma_0=13.8$ deg and where q is a dummy variable. The anisotropy factor relates the relative magnitude of perpendicular and parallel forces, and in RFT formulations of viscous fluids is approximately a constant, 2. In the granular 'frictional fluid' (Maladen et al., 2009; Maladen et al., 2011b), the anisotropy factor has an angular dependence.

The force acting on the blunt head is given by:

$$d\vec{F} = 4k\rho g r^2 \langle z \rangle [f(\hat{T} \cdot \hat{v})\hat{T} + (\hat{N} \cdot \hat{v})\hat{N}], \tag{4}$$

where the direction vectors are taken at the front end of the swimmer's centerline.

To numerically solve the force and torque balance on the swimmer, an iterative approach was employed to determine the infinitesimal translation and rotation of the swimmer from an infinitesimal undulation. The force and torque balances provide three equations, which are used to solve for the two

in-plane velocities and the rotational velocity. To facilitate the numerics, we use the approximation $\hat{v} = \lim_{w \rightarrow 0} (2/\pi) \arctan(v/w) \hat{v}/v$, and iteratively calculate the motion from the force and torque balances with decreasing w .

To account for the lower friction coefficient of the sand snake skin, the tangential forces of the model were reduced accordingly (see supplementary material Fig. S1). The simulation tracked the instantaneous velocity of each segment, which is used in the slip angle calculations, along with the net displacement and expended work to determine the undulatory efficiency, η_u and CoT. We estimate the resulting numerical error in displacement and work for our results to be no more than 2%.

Fitting techniques: B-splines

Snake and sandfish body midline markers were fit with a B-spline function at every time instant during subsurface sand-swimming. The B-spline is a technique that fits a parameterized curve to a set of points in order to represent the underlying smooth function. It does so by solving for the coefficients α_i of a set of basis functions, to estimate the best fit polynomial function (Umar et al., 1991). The B-spline function is described by:

$$x(t) = \sum_{i=1}^N \alpha_i \phi_i^n(t), \quad (5)$$

where $\phi_i^n(t)$ are the basis functions, N are the number of basis functions used and n is the order of the basis function. The coefficients α_i are determined by minimizing the energy function:

$$E = \frac{1}{2} \left\| x(t) - \sum_{i=1}^N \alpha_i \phi_i^n(t) \right\|^2 + \frac{1}{2} \lambda_b \alpha^T \nabla^2 \alpha, \quad (6)$$

where λ_b is a regularization term that controls the smoothness of the fit (Eilers and Marx, 2010), and $\alpha = [\alpha_1 \alpha_2 \dots \alpha_N]^T$.

The number of basis functions defined for each snake was equal to the number of markers along the body (between 26 and 35 for the snake and between 9 and 10 for the sandfish); hence, we were able to fully capture the subjects wide range of motion. These markers were equally spaced along the body at ≈ 1 cm increments for the snake and 0.1 SVL increments for the sandfish. We used 3rd order B-spline basis functions to have smooth and continuous 1st and 2nd order derivatives along the body. A regularization term λ_b of 0.001 was used for all snake and sandfish data.

Body-particle friction effect on forces

Numerical discrete element simulation was used to determine the effect of body-particle friction on parallel and perpendicular forces acting on small intruder moving through an experimentally validated model of 3 mm diameter closely packed glass particles (see Maladen et al., 2011b). A 4 cm-long, 1.6 cm-square rod was dragged such that its long axis was oriented at varying angles (ϕ) with respect to the velocity direction. Only the forces along the length of the rod were considered in analysis; forces on the end-caps were ignored. Body-particle frictions of 0.27 and 0.13 were simulated. As expected, halving the body-particle friction resulted in similar perpendicular forces while parallel forces decreased by 50% (supplementary material Fig. S1).

Acknowledgements

We thank Yang Ding for performing the drag simulations. Thanks to Perrin Schiebel for providing photos of the *Chionactis occipitalis*. Thanks to Kevin and April Young for assistance with collection and care of the *Chionactis occipitalis*.

Competing interests

The authors declare no competing or financial interests.

Author contributions

S.S.S. contributed to the design and implementation of snake and sandfish experiments, and to the kinematic analysis of experimental results. Additionally, she contributed to the written work and figures of this publication. S.A.K. conducted RFT simulations and generated the corresponding figures. He also helped with experimental analysis and the writing on this manuscript. R.M.K. assisted in the design and implementation of the snake experiments. M.S. and advisor, P.A.V., wrote the custom code for automatic kinematic tracking of snake kinematics and provided the custom-written B-Spline fitting program, which aided in obtaining measures of slip. They also contributed to the corresponding written

manuscript detailing the B-Spline fitting methodology. J.M. assisted in obtaining the snakes used in this study, and in the evolutionary interpretation of the results presented in this paper. He contributed to the Introduction and Discussion sections of the written manuscript. D.I.G. helped in all aspects of this research, including the design of experiments, the interpretation of experimental and theoretical results, and the writing and implications of this work.

Funding

This work was supported by National Science Foundation (NSF) Physics of Living Systems (PoLS) grants no. PHY-0749991 and no. PHY-1150760, and ARO grant no. W911NF-11-1-0514 to S.S.S., R.M.K. and D.I.G., and NSF ECS no. 0846750 to M.S. and P.A.V.

Supplementary material

Supplementary material available online at <http://jeb.biologists.org/lookup/suppl/doi:10.1242/jeb.108357/-/DC1>

References

- Alexander, R. M. (2003). *Principles of Animal Locomotion*. Princeton, NJ: Princeton University Press.
- Anderson, J. and Wendt, J. (1995). *Computational Fluid Dynamics*. New York, NY: McGraw-Hill.
- Aristotle (350 BCE). *Historia Animalium*.
- Berri, S., Boyle, J. H., Tassieri, M., Hope, I. A. and Cohen, N. (2009). Forward locomotion of the nematode *C. elegans* is achieved through modulation of a single gait. *Hfsp J.* **3**, 186-193.
- Berthé, R. A., Westhoff, G., Bleckmann, H. and Gorb, S. N. (2009). Surface structure and frictional properties of the skin of the Amazon tree boa *Corallus hortulanus* (Squamata, Boidae). *J. Comp. Physiol. A* **195**, 311-318.
- Blake, R. (2004). Fish functional design and swimming performance. *J. Fish Biol.* **65**, 1193-1222.
- Brandley, M. C., Huelsenbeck, J. P. and Wiens, J. J. (2008). Rates and patterns in the evolution of snake-like body form in squamate reptiles: evidence for repeated re-evolution of lost digits and long-term persistence of intermediate body forms. *Evolution* **62**, 2042-2064.
- Brooks, R. A. (1992). Artificial life and real robots. In *Toward a Practice of Autonomous Systems: Proceedings of the First European Conference on Artificial Life* (ed. F. J. Varela and P. Bourgine), pp. 3. Cambridge, MA: MIT Press.
- Cowles, R. B. (1941). Observations on the winter activities of desert reptiles. *Ecology* **22**, 125-140.
- Cross, J. K. (1979). *Multivariate and Univariate Character Geography in Chionactis (Reptilia: Serpentes)*. Tucson, AZ: University of Arizona.
- Dayton, G. H., Saenz, D., Baum, K. A., Langerhans, R. B. and DeWitt, T. J. (2005). Body shape, burst speed and escape behavior of larval anurans. *Oikos* **111**, 582-591.
- Ding, Y., Sharpe, S. S., Masse, A. and Goldman, D. I. (2012). Mechanics of undulatory swimming in a frictional fluid. *PLoS Comput. Biol.* **8**, e1002810.
- Ding, Y., Sharpe, S. S., Wiesenfeld, K. and Goldman, D. I. (2013). Emergence of the advancing neuromechanical phase in a resistive force dominated medium. *Proc. Natl. Acad. Sci. USA* **110**, 10123-10128.
- Drucker, E. G. and Lauder, G. V. (1999). Locomotor forces on a swimming fish: three-dimensional vortex wake dynamics quantified using digital particle image velocimetry. *J. Exp. Biol.* **202**, 2393-2412.
- Eilers, P. H. C. and Marx, B. D. (2010). Splines, knots, and penalties. *WIREs Comp. Stat.* **2**, 637-653.
- Fish, F. E. and Battle, J. M. (1995). Hydrodynamic design of the humpback whale flipper. *J. Morphol.* **225**, 51-60.
- Fish, F. and Lauder, G. (2006). Passive and active flow control by swimming fishes and mammals. *Annu. Rev. Fluid Mech.* **38**, 193-224.
- Full, R. J. and Koditschek, D. E. (1999). Templates and anchors: neuromechanical hypotheses of legged locomotion on land. *J. Exp. Biol.* **202**, 3325-3332.
- Gans, C. (1975). Tetrapod limbllessness: evolution and functional corollaries. *Am. Zool.* **15**, 455-467.
- Garland, T., Jr and Losos, J. B. (1994). Ecological morphology of locomotor performance in squamate reptiles. In *Ecological Morphology: Integrative Organismal Biology* (ed. P. C. Wainwright and S. M. Reilly), pp. 240-302. Chicago, IL: University of Chicago Press.
- Gravish, N., Umbanhowar, P. B. and Goldman, D. I. (2010). Force and flow transition in plowed granular media. *Phys. Rev. Lett.* **105**, 128301.
- Gray, J. and Lissmann, H. W. (1950). The kinetics of locomotion of the grass-snake. *J. Exp. Biol.* **26**, 354-367.
- Hu, D. L., Nirody, J., Scott, T. and Shelley, M. J. (2009). The mechanics of slithering locomotion. *Proc. Natl. Acad. Sci. USA* **106**, 10081-10085.
- Lauder, G. V. (1981). Form and function: structural analysis in evolutionary morphology. *Paleobiology* **7**, 430-442.
- Lauder, G. V. and Drucker, E. G. (2004). Morphology and experimental hydrodynamics of fish fin control surfaces. *IEEE J. Oceanic Eng.* **29**, 556-571.
- Lauder, G. V., Anderson, E. J., Tangorra, J. and Madden, P. G. (2007). Fish biorobotics: kinematics and hydrodynamics of self-propulsion. *J. Exp. Biol.* **210**, 2767-2780.
- Lee, M. (1998). Convergent evolution and character correlation in burrowing reptiles: towards a resolution of squamate relationships. *Biol. J. Linn. Soc. Lond.* **65**, 369-453.

- Leopold, L. B. (1994). *A View of the River*. Cambridge, MA: Harvard University Press.
- Li, C., Umbanhowar, P. B., Komsuoglu, H., Koditschek, D. E. and Goldman, D. I. (2009). From the Cover: Sensitive dependence of the motion of a legged robot on granular media. *Proc. Natl. Acad. Sci. USA* **106**, 3029-3034.
- Liao, J. C. (2007). A review of fish swimming mechanics and behaviour in altered flows. *Philos. Trans. R. Soc. B* **362**, 1973-1993.
- Lighthill, M. (1971). Large-amplitude elongated-body theory of fish locomotion. *Proc. R. Soc. B* **179**, 125-138.
- Liu, H., Wassersug, R. and Kawachi, K. (1996). A computational fluid dynamics study of tadpole swimming. *J. Exp. Biol.* **199**, 1245-1260.
- Long, J., Jr and Nipper, K. (1996). The importance of body stiffness in undulatory propulsion. *Am. Zool.* **36**, 678-694.
- Maladen, R. D., Ding, Y., Li, C. and Goldman, D. I. (2009). Undulatory swimming in sand: subsurface locomotion of the sandfish lizard. *Science* **325**, 314-318.
- Maladen, R. D., Ding, Y., Umbanhowar, P. B. and Goldman, D. I. (2011a). Undulatory swimming in sand: experimental and simulation studies of a robotic sandfish. *Int. J. Robot. Res.* **30**, 793-805.
- Maladen, R. D., Ding, Y., Umbanhowar, P. B., Kamor, A. and Goldman, D. I. (2011b). Mechanical models of sandfish locomotion reveal principles of high performance subsurface sand-swimming. *J. R. Soc. Interface* **8**, 1332-1345.
- Maladen, R. D., Umbanhowar, P. B., Ding, Y., Masse, A. and Goldman, D. I. (2011c). Granular lift forces predict vertical motion of a sand-swimming robot. In *Proceedings of the 2011 IEEE International Conference on Robotics and Automation (ICRA)*, pp. 1398-1403. New York, NY: IEEE.
- McHenry, M. J. and Jed, J. (2003). The ontogenetic scaling of hydrodynamics and swimming performance in jellyfish (*Aurelia aurita*). *J. Exp. Biol.* **206**, 4125-4137.
- McHenry, M., Pell, C. and Jr, J. (1995). Mechanical control of swimming speed: stiffness and axial wave form in undulating fish models. *J. Exp. Biol.* **198**, 2293-2305.
- Miklosovich, D., Murray, M., Howle, L. and Fish, F. (2004). Leading-edge tubercles delay stall on humpback whale (*Megaptera novaeangliae*) flippers. *Phys. Fluids* **16**, L39-L42.
- Mosauer, W. (1932). Adaptive convergence in the sand reptiles of the Sahara and of California: a study in structure and behavior. *Copeia* **72-78**.
- Mosauer, W. (1933). Locomotion and diurnal range of *Sonora occipitalis*, *Crotalus cerastes*, and *Crotalus atrox* as seen from their tracks. *Copeia* **1933**, 14-16.
- Mosauer, W. (1936). The reptilian fauna of sand dune areas of the vicaino desert and of northwestern lower California. *Occas. Pap. Mus. Zool. Univ. Mich.* **329**, 1-25.
- Norris, K. S. and Kavanau, J. L. (1966). The burrowing of the western shovel-nosed snake, *Chionactis occipitalis* Hallowell, and the undersand environment. *Copeia* **1966**, 650-664.
- Pedley, T. J. and Hill, S. J. (1999). Large-amplitude undulatory fish swimming: fluid mechanics coupled to internal mechanics. *J. Exp. Biol.* **202**, 3431-3438.
- Pfeifer, R., Lungarella, M. and Iida, F. (2007). Self-organization, embodiment, and biologically inspired robotics. *Science* **318**, 1088-1093.
- Rieppel, O. (1988). A review of the origin of snakes. In *Evolutionary Biology*, pp. 37-130. New York, NY: Springer.
- Russell, E. S. (1917). *Form and Function: A Contribution to the History of Animal Morphology*. New York, NY: E. P. Dutton.
- Sfakiotakis, M., Lane, D. M. and Davies, J. B. C. (1999). Review of fish swimming modes for aquatic locomotion. *IEEE J. Oceanic Eng.* **24**, 237-252.
- Sharpe, S. S., Ding, Y. and Goldman, D. I. (2013). Environmental interaction influences muscle activation strategy during sand-swimming in the sandfish lizard *Scincus scincus*. *J. Exp. Biol.* **216**, 260-274.
- Sites, J. W., Jr, Reeder, T. W. and Wiens, J. J. (2011). Phylogenetic insights on evolutionary novelties in lizards and snakes: sex, birth, bodies, niches, and venom. *Annu. Rev. Ecol. Evol. Syst.* **42**, 227-244.
- Tytell, E. D. and Lauder, G. V. (2004). The hydrodynamics of eel swimming: I. Wake structure. *J. Exp. Biol.* **207**, 1825-1841.
- Tytell, E. D., Borazjani, I., Sotiropoulos, F., Baker, T. V., Anderson, E. J. and Lauder, G. V. (2010). Disentangling the functional roles of morphology and motion in the swimming of fish. *Integr. Comp. Biol.* **50**, 1140-1154.
- Umar, A. S., Wu, J., Strayer, M. R. and Bottcher, C. (1991). Basis-spline collocation method for the lattice solution of boundary value problems. *J. Comp. Phys.* **93**, 426-448.
- Wainwright, P. C. and Reilly, S. M. (1994). *Ecological Morphology: Integrative Organismal Biology*. Chicago, IL: University of Chicago Press.
- Walker, J. A. and Westneat, M. W. (2000). Mechanical performance of aquatic rowing and flying. *Proc. R. Soc. B* **267**, 1875-1881.
- Webb, P. W. and Weihs, D. (1986). Functional locomotor morphology of early life history stages of fishes. *Trans. Am. Fish. Soc.* **115**, 115-127.
- Wiens, J. J. and Slingluff, J. L. (2001). How lizards turn into snakes: a phylogenetic analysis of body-form evolution in anguid lizards. *Evolution* **55**, 2303-2318.
- Wiens, J. J., Brandley, M. C. and Reeder, T. W. (2006). Why does a trait evolve multiple times within a clade? Repeated evolution of snakelike body form in squamate reptiles. *Evolution* **60**, 123-141.
- Wilson, S. K. (2012). *Australian Lizards: A Natural History*. Collingwood, VIC: Csiro Publishing.
- Yim, M., Shen, W.-M., Salemi, B., Rus, D., Moll, M., Lipson, H., Klavins, E. and Chirikjian, G. S. (2007). Modular self-reconfigurable robot systems (grand challenges of robotics). *IEEE Robot. Autom. Mag.* **14**, 43-52.

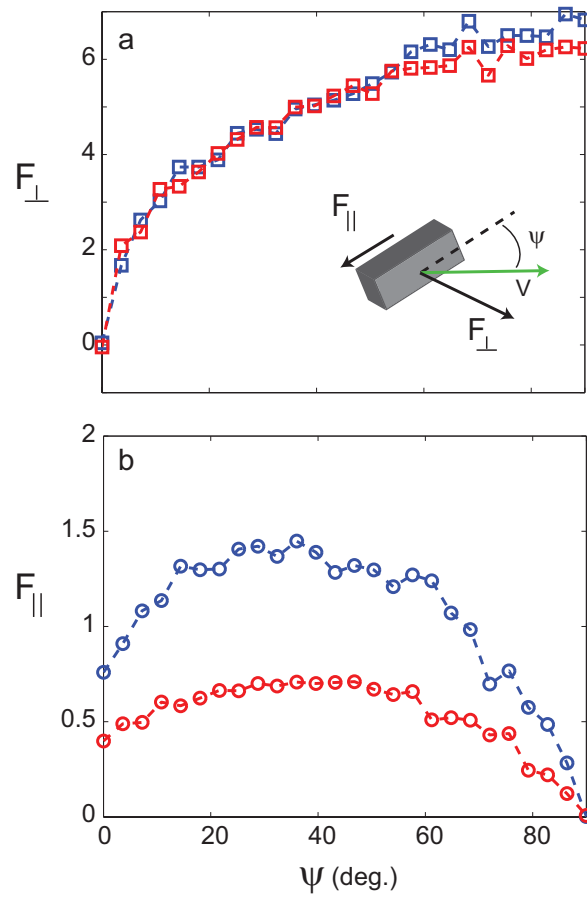


Figure S1: (a) Perpendicular and (b) parallel forces on a square cross-section rod (width & height = 16 mm, length = 40 mm) dragged through 3 mm glass closely packed particles in simulation as a function of the angle, ψ , between the velocity direction and the rod axis. The blue markers correspond to forces on a rod with body-grain coefficient of friction of 0.27 and the red markers correspond to a body-grain friction of 0.13. Courtesy of Yang Ding.

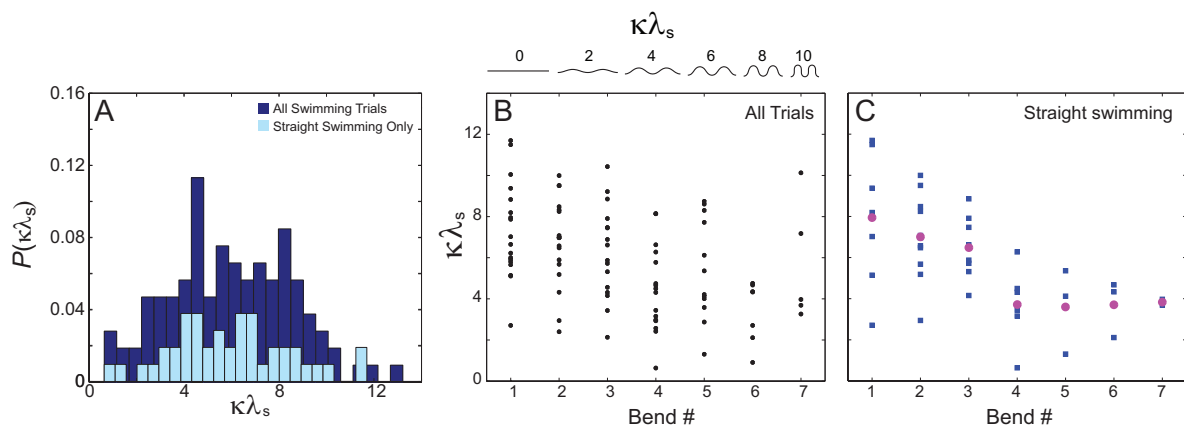


Figure S2: The local relative curvature, $\kappa\lambda_s$, during straight and turning snake swimming. (A) Distribution of $\kappa\lambda_s$ for all trials (dark bars) and for 'straight' swimming (light blue bars) in which the average body moves along a linear trajectory. In this analysis, each local curvature measured within a trial and across trials is considered an independent datum. (B) $\kappa\lambda_s$ and corresponding bend number for all trials (both turning and straight). Bend number corresponds to the number of half wave lengths along the body after the animal has entered the medium (i.e. bend number 1 is the first half wave visible in X-ray in which that portion of the body is buried). Because the animal is moving deeper into the media, higher bend number corresponds to that portion of the body having a deeper burial depth. (C) $\kappa\lambda_s$ vs. bend number during straight swimming *only*. Magenta circles show the average $\kappa\lambda_s$ at each bend for straight swimming. The maximum $\kappa\lambda_s$ decreased for straight swimming while the minimum stayed approximately constant with increasing bend number.



Movie 1. (A) Shovel-nosed snake (*Chionactis occipitalis*) burying into dry granular media composed of 0.3 mm diameter glass particles. (B) Video with panels showing shovel-nosed snake burial and swimming, from left to right: Visible light (left panel), x-ray with overlay with B-Spline fit to the body midline (mid panel) derived from tracked markers (right panel). All video played real time.

Table S1: Means and \pm s.d. for kinematic parameters.

Measured Parameters	symbol	<i>C. chionactis</i>			<i>S. scincus</i>		
		CP	LP	T-test	CP	LP	T-test
Relative curvature*	$\overline{\kappa\lambda_s}$	6.2 \pm 1.3	6.0 \pm 1.3	$P > 0.84$	7.4 \pm 1.3	7.5 \pm 0.8	$P > 0.75$
Undulation number	$\overline{\xi}$	3.50 \pm 0.52	3.53 \pm 0.85	$P > 0.93$	1.04 \pm 0.14	0.99 \pm 0.06	$P > 0.13$
Average slip angle	$\overline{\beta_s}$	6.0 \pm 1.1	6.9 \pm 1.6	$P > 0.2$	21.9 \pm 4.0	21.2 \pm 3.5	$P > 0.51$
Undulation Efficiency	η_u	0.60 \pm 0.06	0.57 \pm 0.09	$P > 0.48$	0.28 \pm 0.05	0.27 \pm 0.08	$P > 0.63$

*Relative curvature was averaged across all bends visible along the body.

The mean and s.d. represent across trial values